Journal of Sound and Vibration 488 (2020) 115637

Contents lists available at ScienceDirect

Journal of Sound and Vibration

journal homepage: www.elsevier.com/locate/jsv

Entropy noise modelling in 2D choked nozzle flows

Maxime Huet[a,*], Ariane Emmanuelli[a,b], Thomas Le Garrec[a]

[a] DAAA, ONERA, Université Paris Saclay, Châtillon F-92322, France
[b] LMFA - Laboratoire de Mécanique des Fluides et d'Acoustique, Ecole Centrale de Lyon, 36 Avenue Guy de Collongue, Ecully Cedex, 69134, France

ARTICLE INFO

Article history:
Received 28 February 2020
Revised 28 July 2020
Accepted 11 August 2020
Available online 12 August 2020

Keywords:
Entropy noise
Low-order model
Nozzle
Choked flow

ABSTRACT

Entropy noise is produced when temperature fluctuations (entropy spots) are accelerated by the mean flow, through a nozzle or a turbine stage for instance. When it propagates outside the engine it contributes to community noise and may generate thermoacoustic instabilities when reflected back towards the combustor, hence the need for its modelling. Among all the inviscid models proposed in the literature, only the one developed by ONERA takes into account the 2D nature of the mean flow and the radial deformation of the entropy waves through the nozzle, which plays a crucial role in noise generation (Emmanuelli et al., J. Sound Vib., vol. 472, 2020, pp. 115163). This model has been validated in the subsonic regime and is extended in the present work to 2D supercritical configurations, without and with a normal shock in the diffuser. Modelled transfer functions are validated by comparison with reference data obtained with computational aeroacoustics simulations and excellent agreement is found between the simulations and the model. The contribution of the shear dispersion of the entropy wave to noise generation is evidenced and the failure of the quasi-1D models, which do not account for the radial deformation of the entropy fluctuations, is illustrated. Noise scattering through the nozzle is also investigated. The 2D model is found to correctly recover the simulated transmitted and reflected acoustic waves through the nozzle. Quasi-1D solutions are also found to collapse with the reference simulations, which indicates that 2D mean flow effects are negligible for the propagation of the acoustic waves through the nozzle.

1. Introduction

The increase of air traffic combined with urban densification around airports and heliports led to the rise of the number of people subject to discomfort. Amongst others, noise pollution has become an environmental issue with more and more severe regulations [1]. The main contributors to aircraft noise are historically the jet and the fan. Jet noise has been strongly reduced in particular by using ultra-high-bypass ratio turbofan engines [2] whereas liners and optimised fan blade geometries helped decrease fan noise. Other noise sources that were previously masked now emerge. It is for instance the case of combustion noise during approach in the medium frequency range [3,4]. The contribution of combustion to the total engine noise is even more important for helicopter engines due to the absence of the jet and the fan. In addition to community noise issues, the noise produced inside the combustor may couple with the flame and generate thermoacoustic instabilities [5,6], which might damage the combustor or even lead to the complete destruction of the engine. To handle these problems,

* Corresponding author:
E-mail address: maxime.huet@onera.fr (M. Huet).

https://doi.org/10.1016/j.jsv.2020.115637

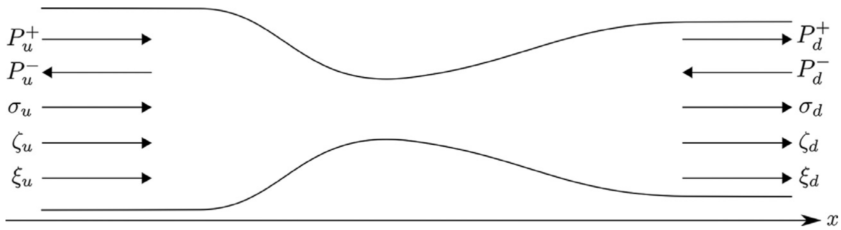

Fig. 1. General sketch of a nozzle with all incoming and outgoing waves.

the use of low-order models for a quick and reliable estimation of combustion generated noise during engine conception reveals to be crucial.

The contribution of combustion noise was first evidenced in the 1970s when engine noise was found to be higher than the sole contribution of the jet [7]. First referred to as excess noise [8], this additional noise was then associated with the combustion process and is now called core noise [9] or combustion noise [10]. Early theoretical analysis was provided by Bragg [11] and Strahle [12] and this noise was shown to have two distinct origins: direct noise refers to pressure fluctuations generated by the unsteady heat release of the flame [13,14] while indirect noise corresponds to additional noise produced when inhomogeneities such as hot/cold spots (entropy noise), vorticity fluctuations (vorticity noise) or mixture heterogeneities (compositional noise) are accelerated by the mean flow [15–18]. In gas turbines, mean flow acceleration is primarily caused by the turbine stages located downstream of the combustor. The flow inside turbine stages is however complex and makes the development of models and experiments difficult for the study of indirect noise generation. Simplified configurations are usually investigated by accelerating the flow thanks to a converging-diverging nozzle, which provides a more fundamental framework for analytical and experimental studies [19–21]. A general sketch of a nozzle with the different waves present in the flow is reproduced in Fig. 1, where $P^{\pm}$ correspond to the progressive and regressive acoustic waves, σ to the entropy wave, ζ to the vorticity wave, ξ to the compositional wave and subscripts $(\,\cdot\,)_u$ and $(\,\cdot\,)_d$ to quantities upstream and downstream of the nozzle, respectively. When a perturbation enters the nozzle, it leads to a loss of balance to which the flow reacts by generating fluctuations, typically of acoustic nature. Entropy noise is for instance the result of the loss of pressure balance as entropy waves are expanded in accelerated flow [22,23]. The objective of low-order models is to determine these generated waves. They are usually evaluated as transfer functions, *i.e.* ratios between the outgoing generated wave and the ingoing forcing one.

Among all the models available in the literature for nozzle flows, the most widely used is certainly the one proposed by Marble and Candel [19]. The authors assume a quasi-1D inviscid flow, where vorticity and compositional fluctuations are absent and acoustic and entropy waves are planar. In the first part of their paper, they consider a compact nozzle, where all wavelengths are large compared to the nozzle length so that it can be treated as a discontinuity. Conservation relations for mass, stagnation temperature and entropy through the nozzle are used to express the generated waves as a function of the incoming ones. This model was recently extended to nonlinear perturbations by Huet and Giauque [24,25] and to azimuthal modes and vorticity waves in thin annular ducts by Mahmoudi et al. [26]. In the second part of their paper, Marble and Candel also illustrate a non-compact approach for a supercritical nozzle with a linear velocity profile, where the generated noise depends of the frequency f of the perturbation. The linearized Euler equations are non-dimensionalised and an ordinary differential equation is obtained for the pressure fluctuation, which can be solved analytically. This method was later adapted to choked nozzles and supersonic diffusers with a shock in the diffuser by Moase et al. [27] and to nozzles with an arbitrary shape by Giauque et al. [28] and Huet et al. [29]. This approach proved efficient to design a nozzle with optimal indirect noise generation through the use of a genetic algorithm, for instance [30]. In a different way, Mahmoudi et al. [31] discretised the nozzle as a succession of ducts of constant radii and used the compact solutions to link acoustic, entropy and vorticity waves (including azimuthal modes) between successive elements.

Other approaches to deal with non-compact nozzles were proposed by Bohn [32] and Duran and Moreau [33]. Assuming a harmonic regime and subsonic flow, Bohn reduced the quasi-1D linearized Euler equations to a system of coupled ordinary differential equations to be integrated numerically along the nozzle axis to provide the transfer functions. In addition, asymptotic analytical solutions of the transfer functions were provided for $f \to +\infty$ considering a linear velocity profile. Duran and Moreau, on the other hand, recast the quasi-1D linearized Euler equations to write a differential system over the fluctuations of mass flow rate, stagnation temperature and entropy, solved using the Magnus expansion. This modelling handles both subsonic and choked nozzle flows, with a possible shock in the diffuser. This approach was later extended by Duran and Morgans to deal with circumferential and vorticity waves in annular ducts [34].

All the above-mentioned modellings assume the gas is calorically perfect, that is to say heat capacities are independent of temperature. When the flow is strongly accelerated through the nozzle, temperature variation might become important and heat capacity variations may not be negligible anymore. The influence of temperature-dependent heat capacities has been investigated numerically by Huet [35] and was shown to have a negligible contribution in the generation of indirect combustion noise.

A validation of these models has been achieved through comparisons with experimental data. Huet [36] verified for instance the noise scattered through subsonic and choked nozzle flows (acoustic forcing) for frequencies up to 3 kHz using the experimental results of Knobloch et al. from the Hot Acoustic Test rig [21], designed and operated by DLR. This validation particularly confirms that acoustic waves remain one-dimensional through the nozzle. The entropy-generated noise has also been addressed for the compact nozzle in the choked flow framework by Leyko et al. using the Entropy Wave Generator (EWG) [20], also developed and operated by DLR. It is however expected that quasi-1D models fail to predict non-compact entropy noise, because for such frequencies the entropy waves are deformed during their convection through the nozzle and do not remain 1D. This deformation was first considered by Zheng et al. [37], who predicted a modification of the noise source terms distribution inside the nozzle and derived a 2D model to deal with the radial deformation of the entropy fluctuations [38]. A first illustration of the relevance of the 2D model was achieved through comparisons with a Large Eddy Simulation of a subsonic nozzle flow [39], where the overestimation of the thermoacoustic transfer functions (generation of acoustics from entropy) predicted by the quasi-1D model was drastically reduced with the 2D model. These comparisons were complemented by the numerical work of Emmanuelli et al., who obtained an excellent quantitative agreement between high-order computational aeroacoustics (CAA) simulations and the 2D model [38,40]. A similar radial deformation of the entropy waves and subsequent failure of the quasi-1D models to predict the generated noise was observed numerically by Becerril [41] for the subsonic EWG test case.

The 2D model presented in [38] is limited to subsonic nozzle flows. In the present article, it is extended to choked flows, without or with a shock in the diffuser. The analytical modelling is detailed in Section 2. Basic assumptions are first recalled and discussed, after what the model equations are derived in the general case and discretised for numerical resolution. Boundary conditions are also addressed in this section. Discretised equations are recast in matrix form in Section 3 and a numerical resolution procedure is proposed for the different flow regimes. The general form of the matrix system corresponds to the subsonic flow configuration, detailed first, and additional terms related to the choked nozzle flow and the presence of the shock in the diffuser are included afterwards. Section 4 presents numerical validations for a choked flow with a shock in the diffuser while conclusions are drawn in Section 5.

2. Analytical modelling

The nozzle is oriented along the x axis and the fluid flows towards the increasing x direction without swirl motion. The flow is assumed to be inviscid, so that the Euler equations are considered. Mean flow and perturbations are axisymmetric and the amplitudes of the fluctuations are sufficiently small for the flow equations to be linearised. Chu and Kovásznay showed perturbations of acoustic, entropic and vorticity nature are present in such flows [42]. They are decoupled in a uniform flow but couple in the presence of flow gradients. The nozzle radius is supposed to be small enough for the radial acoustic modes to be cut-off for the considered frequencies, typically below a few kHz. To first order, entropy fluctuations are convected by the mean flow without attenuation, except through a shock where their amplification/attenuation is taken into account (see Section 3.3). Finally, vorticity is neglected. For inviscid flows, vorticity is produced by the baroclinic torque caused by the radial deformation of the entropy waves [34]. Recent simulations showed that its contribution to generated noise is indeed negligible when viscosity is not considered [40,41]. From these hypotheses, the only perturbations present are entropic and acoustic, the latter being in addition assumed one-dimensional.

The objective of the present 2D model is to compute the acoustic and thermoacoustic transfer functions of the nozzle, *i.e.* the noise leaving the nozzle from both extremities as a function of the acoustic or entropic forcing, both in amplitude and phase. Their evaluation requires the separation of the different waves present in the domain, namely the entropy and acoustic waves, in the ducts upstream and downstream of the nozzle. The entropy wave is directly obtained from the entropy fluctuation:

$$\sigma = \frac{s'}{c_p} \tag{1}$$

with s' the entropy fluctuation and c_p the heat capacity at constant pressure, and acoustic waves are evaluated using the Riemann invariants:

$$P^{\pm} = \frac{1}{2}\left(\frac{p'}{\gamma\overline{p}_0} \pm \frac{\overline{\rho_0 c_0}}{\gamma\overline{p}_0}u'_x\right) \tag{2}$$

where P^+ and P^- correspond to the progressive and regressive acoustic waves, p, u_x, ρ and c to the pressure, axial velocity, density and sound velocity, $\gamma = c_p/c_v$ to the adiabatic coefficient (c_v being the heat capacity at constant volume), subscript $(\,\cdot\,)_0$ to a mean flow quantity and superscript $(\,\cdot\,)'$ to a perturbation. The overlined quantities $\overline{(\cdot)}$ indicate flow variables averaged over the duct cross section A, as defined in Eq. (3). This averaging is not mandatory in upstream and downstream ducts where the flow is uniform, but this notation is kept for the sake of coherence with the rest of the paper.

$$\overline{f} = \frac{1}{A}\int_A f dA \tag{3}$$

2.1. Flow equations in the nozzle

The mass conservation and momentum equations write [38]

$$\frac{\partial \overline{\rho}}{\partial t} + \frac{\partial \overline{\rho u_x}}{\partial x} = -\frac{1}{A}\overline{\rho u_x}\frac{dA}{dx}, \tag{4}$$

$$\frac{\partial u_x}{\partial t} + u_x\frac{\partial u_x}{\partial x} + u_r\frac{\partial u_x}{\partial r} = -\frac{1}{\rho}\frac{\partial p}{\partial x}, \tag{5}$$

with t the time and u_r the radial velocity. These equations are first linearised using the model's assumptions ($\overline{p'} = p'$, $\overline{u'_x} = u'_x$, $u'_r = 0$) and the entropy relation $s'/c_p = p'/\gamma p - \rho'/\rho$, then switched into the frequency domain. Under the harmonic regime hypothesis, the fluctuations write

$$u'_x(x,t) = \mathrm{Re}\left[\hat{u}(x)\mathrm{e}^{i\omega t}\right], \tag{6}$$

$$p'(x,t) = \mathrm{Re}\left[\hat{p}(x)\mathrm{e}^{i\omega t}\right], \tag{7}$$

$$\frac{s'}{c_p}(x,t) = \mathrm{Re}\left[\hat{\sigma}(x)\mathrm{e}^{i\omega t}\right], \tag{8}$$

where $\hat{u}$, $\hat{p}$ and $\hat{\sigma}$ are the complex amplitudes of the axial velocity, pressure and non-dimensional entropy fluctuations, ω is the angular frequency and $Re[\,\cdot\,]$ stands for the real part of a complex number. The mass conservation and section-averaged momentum equations finally write

$$\left(A\overline{\left(\frac{1}{c_0^2}\right)}i\omega + \frac{d}{dx}\left[A\overline{\left(\frac{u_{0x}}{c_0^2}\right)}\right]\right)\hat{p} + \left[A\overline{\left(\frac{u_{0x}}{c_0^2}\right)}\right]\frac{d\hat{p}}{dx} + \frac{dA\overline{\rho}_0}{dx}\hat{u} + A\overline{\rho}_0\frac{d\hat{u}}{dx} = \frac{d}{dx}\left[A\overline{(\rho_0 u_{0x})\hat{\sigma}}\right] + Ai\omega\overline{\rho_0\hat{\sigma}}, \tag{9}$$

$$\left[\overline{\left(\frac{u_{0x}}{\gamma p_0}\frac{\partial u_{0x}}{\partial x}\right)} + \overline{\left(\frac{u_{0r}}{\gamma p_0}\frac{\partial u_{0x}}{\partial r}\right)}\right]\hat{p} + \overline{\left(\frac{1}{\rho_0}\right)}\frac{d\hat{p}}{dx} + \left[i\omega + \overline{\left(\frac{\partial u_{0x}}{\partial x}\right)}\right]\hat{u} + \overline{u}_{0x}\frac{d\hat{u}}{dx} = \overline{\left[u_{0x}\frac{\partial u_{0x}}{\partial x} + u_{0r}\frac{\partial u_{0x}}{\partial r}\right]\hat{\sigma}}. \tag{10}$$

2.2. Numerical discretisation

Eqs. (9) -(10) involve the mean flow variables and the fluctuating terms $\hat{u}$, $\hat{p}$ and $\hat{\sigma}$. The mean flow variables are input data provided by a simulation of the steady inviscid flow, for instance. The entropy fluctuation is assumed to be convected by the mean flow without diffusion and, in the absence of a shock, it is simply computed using the average velocity field; its numerical evaluation is detailed in Section 2.3. The system is finally composed of 2 equations and 2 unknowns and can be solved numerically.

System resolution is achieved using a spatial discretisation along the flow direction (x). The unsteady flow variables $\hat{u}$ and $\hat{p}$ are sought at the nodes k of the grid, $k = 1\ldots n$, and Eqs. (9)-(10) are evaluated at the centre of the $(n-1)$ elements. The perturbed flow variables and their axial derivatives are evaluated at the centre of each element using relations (11)-(12):

$$f_{k+1/2} = \frac{f_{k+1} + f_k}{2}, \tag{11}$$

$$\frac{d}{dx}f_{k+1/2} = \frac{f_{k+1} - f_k}{\Delta x_{k+1/2}}, \tag{12}$$

where $\Delta x_{k+1/2}$ is the size of the element $k+1/2$, bounded by the nodes k and $k+1$. Using this discretisation, continuity and momentum equations write

$$\lambda^1_{k+1/2}\hat{p}_k + \lambda^2_{k+1/2}\hat{u}_k + \lambda^3_{k+1/2}\hat{p}_{k+1} + \lambda^4_{k+1/2}\hat{u}_{k+1} = \hat{S}^C_{k+1/2}, \tag{13}$$

$$\phi^1_{k+1/2}\hat{p}_k + \phi^2_{k+1/2}\hat{u}_k + \phi^3_{k+1/2}\hat{p}_{k+1} + \phi^4_{k+1/2}\hat{u}_{k+1} = \hat{S}^M_{k+1/2}, \tag{14}$$

where $\hat{u}_k$ and $\hat{p}_k$ correspond to the velocity and pressure amplitudes at node k and $\lambda^j_{k+1/2}$, $\phi^j_{k+1/2}$, $\hat{S}^C_{k+1/2}$, $\hat{S}^M_{k+1/2}$ to the area-averaged mean flow quantities and entropy-related source terms evaluated inside element $k+1/2$. These quantities write

$$\lambda^1_{k+1/2} = \left(\frac{1}{2}\left[A\overline{\left(\frac{1}{c_0^2}\right)}i\omega + \frac{d}{dx}\left[A\overline{\left(\frac{u_{0x}}{c_0^2}\right)}\right]\right] - \frac{A}{\Delta x}\overline{\left(\frac{u_{0x}}{c_0^2}\right)}\right)_{k+1/2}, \tag{15}$$

$$\lambda^2_{k+1/2} = \left(\frac{1}{2} \frac{dA\overline{\rho}_0}{dx} - \frac{A\overline{\rho}_0}{\Delta x} \right)_{k+1/2}, \tag{16}$$

$$\lambda^3_{k+1/2} = \left(\frac{1}{2} \left[A\overline{\left(\frac{1}{c_0^2} \right)} i\omega + \frac{d}{dx} \left[A\overline{\left(\frac{u_{0x}}{c_0^2} \right)} \right] \right] + \frac{A}{\Delta x} \overline{\left(\frac{u_{0x}}{c_0^2} \right)} \right)_{k+1/2}, \tag{17}$$

$$\lambda^4_{k+1/2} = \left(\frac{1}{2} \frac{dA\overline{\rho}_0}{dx} + \frac{A\overline{\rho}_0}{\Delta x} \right)_{k+1/2}, \tag{18}$$

$$\phi^1_{k+1/2} = \left(\frac{1}{2} \left[\overline{\left(\frac{u_{0x}}{\gamma p_0} \frac{\partial u_{0x}}{\partial x} \right)} + \overline{\left(\frac{u_{0r}}{\gamma p_0} \frac{\partial u_{0x}}{\partial r} \right)} \right] - \frac{1}{\Delta x} \overline{\left(\frac{1}{\rho_0} \right)} \right)_{k+1/2}, \tag{19}$$

$$\phi^2_{k+1/2} = \left(\frac{1}{2} \left[i\omega + \overline{\left(\frac{\partial u_{0x}}{\partial x} \right)} \right] - \frac{1}{\Delta x} \overline{u}_{0x} \right)_{k+1/2}, \tag{20}$$

$$\phi^3_{k+1/2} = \left(\frac{1}{2} \left[\overline{\left(\frac{u_{0x}}{\gamma p_0} \frac{\partial u_{0x}}{\partial x} \right)} + \overline{\left(\frac{u_{0r}}{\gamma p_0} \frac{\partial u_{0x}}{\partial r} \right)} \right] + \frac{1}{\Delta x} \overline{\left(\frac{1}{\rho_0} \right)} \right)_{k+1/2}, \tag{21}$$

$$\phi^4_{k+1/2} = \left(\frac{1}{2} \left[i\omega + \overline{\left(\frac{\partial u_{0x}}{\partial x} \right)} \right] + \frac{1}{\Delta x} \overline{u}_{0x} \right)_{k+1/2}, \tag{22}$$

$$\hat{S}^C_{k+1/2} = \left(\frac{d}{dx} \left[A\overline{\left(\rho_0 u_{0x} \hat{\sigma} \right)} \right] + Ai\omega \overline{\left(\rho_0 \hat{\sigma} \right)} \right)_{k+1/2}, \tag{23}$$

$$\hat{S}^M_{k+1/2} = \overline{\left(\left[u_{0x} \frac{\partial u_{0x}}{\partial x} + u_{0r} \frac{\partial u_{0x}}{\partial r} \right] \hat{\sigma} \right)}_{k+1/2}. \tag{24}$$

2.3. Computation of the entropy fluctuation and related source terms

For inviscid flow fields, outside of shocks entropy is a quantity convected by the mean flow without attenuation or distortion. Its fluctuation can hence be evaluated theoretically as

$$\frac{s'}{c_p}(l,t) = \frac{s'}{c_p}\left(l = 0, t - \int_0^l \frac{d\zeta}{u_0(\zeta)} \right) \tag{25}$$

with u the velocity norm and where the integration from 0 to l is performed along a streamline of the flow. In the harmonic regime, this equation reduces to

$$\hat{\sigma}(l) = \hat{\sigma}(l = 0) \exp\left(-i\omega \int_0^l \frac{d\zeta}{u_0(\zeta)} \right) \tag{26}$$

with $\hat{\sigma}(l = 0)$ the complex amplitude of the entropy fluctuation. Practically, the computation of entropy fluctuations is performed as follows. A given number of particles are seeded at the geometry inlet and convected through the nozzle flow to generate streamlines and streamtubes, bounded by two successive streamlines. The flow is considered radially constant inside each streamtube and the entropy fluctuation at node k in the j^{th} streamtube is computed as

$$\hat{\sigma}_{k,j} = \hat{\sigma}^0_j e^{i\varphi_{k,j}}, \qquad \varphi_{k,j} = -\omega \int_0^l \frac{d\zeta}{u_0(\zeta)}, \tag{27}$$

with $\hat{\sigma}^0_j$ the initial amplitude of the entropy fluctuation in the j^{th} streamtube. Using Eq. (27), the entropy-related source terms $\hat{S}^C_{k+1/2}$ and $\hat{S}^M_{k+1/2}$ in Eqs. (23)-(24) rewrite

$$\hat{S}^C_{k+1/2} = \sum_{j=1}^{nj} \mu^j_{k+1/2} \hat{\sigma}^0_j, \tag{28}$$

$$\hat{S}^M_{k+1/2} = \sum_{j=1}^{nj} \nu^j_{k+1/2} \hat{\sigma}^0_j, \tag{29}$$

with

$$\mu^j_{k+1/2} = \frac{\left(A_j \rho_{0,j} u_{0x,j}\right)_{k+1} e^{i\varphi_{k+1,j}} - \left(A_j \rho_{0,j} u_{0x,j}\right)_k e^{i\varphi_{k,j}}}{\Delta x_{k+1/2}} + i\omega \left(A_j \rho_{0,j}\right)_{k+1/2} e^{i\varphi_{k+1/2,j}}, \tag{30}$$

$$\nu^j_{k+1/2} = \left(\frac{A_j}{A}\left[u_{0x,j}\frac{\partial u_{0x,j}}{\partial x} + u_{0r,j}\frac{\partial u_{0x,j}}{\partial r}\right]\right)_{k+1/2} e^{i\varphi_{k+1/2,j}}, \tag{31}$$

where nj is the number of streamtubes and A_j the section of the j^{th} streamtube.

2.4. Boundary conditions

The boundary conditions physically express the acoustic waves entering the domain from both extremities. These waves can have two separate origins: they can be either reflections of the outgoing waves on the boundaries or acoustic excitations imposed by the user, $\hat{P}^+_{1f}$ and $\hat{P}^-_{nf}$ (for subsonic outlets), where indices 1 and n correspond to the acoustic waves at nozzle inlet and outlet. In the model, acoustic reflections on the boundaries are supposed to be nil and boundary conditions represent the acoustic excitations imposed by the user. A general method to take into account the contribution of reflection coefficients on the generated noise is presented in Appendix A. Without reflections, the non-dimensional form of the acoustic wave entering the domain from the upstream boundary writes, using Eq. (2):

$$P^+_1 = P^+_{1f} = \frac{1}{2}\left(\frac{\hat{p}}{\gamma \overline{p}_0} + \frac{\overline{\rho_0 c_0}}{\gamma \overline{p}_0}\hat{u}\right)_1. \tag{32}$$

For a subsonic outlet, the acoustic wave entering the domain from the downstream boundary writes, in a similar way:

$$P^-_n = P^-_{nf} = \frac{1}{2}\left(\frac{\hat{p}}{\gamma \overline{p}_0} - \frac{\overline{\rho_0 c_0}}{\gamma \overline{p}_0}\hat{u}\right)_n. \tag{33}$$

3. Computation of the transfer functions

The analytical developments presented above are recast into a matrix form for numerical resolution. This resolution is performed with the in-house code CHEOPS-Nozzle (non-compact harmonic entropy noise predictions). The matrix systems are detailed hereafter for the subsonic and supersonic configurations.

3.1. Subsonic nozzle flow

After discretisation of the nozzle into $n-1$ axial elements bounded by n nodes, Eq. (13)-(14) and (32)-(33) correspond to a linear system of $2n+nj$ equations with $2n+nj$ unknowns. To be solved numerically, it is recast in the matrix form of Eq. (34):

$$\begin{pmatrix}
\left(\frac{1}{2\gamma\overline{p}_0}\right)_1 & \left(\frac{\overline{\rho_0 c_0}}{2\gamma\overline{p}_0}\right)_1 & 0 & .. & .. & .. & .. & .. & .. & .. \\
 & & & & & & \mathcal{A} & & \mathcal{S} & \\
.. & .. & .. & .. & 0 & \left(\frac{1}{2\gamma\overline{p}_0}\right)_n & -\left(\frac{\overline{\rho_0 c_0}}{2\gamma\overline{p}_0}\right)_n & 0 & .. & .. \\
.. & .. & .. & .. & .. & .. & 0 & & & \\
\vdots & & & & & & \vdots & & & \mathcal{I} \\
.. & .. & .. & .. & .. & .. & 0 & & &
\end{pmatrix}
\begin{pmatrix} \hat{P} \\ \\ \hat{\sigma}^0 \end{pmatrix}
=
\begin{pmatrix} \hat{P}^f \\ \\ \hat{\sigma}^f \end{pmatrix} \tag{34}$$

with

$$\mathcal{A}=\begin{pmatrix} \lambda^1_{3/2} & \lambda^2_{3/2} & \lambda^3_{3/2} & \lambda^4_{3/2} & 0 & .. & .. & .. & .. & .. \\ \phi^1_{3/2} & \phi^2_{3/2} & \phi^3_{3/2} & \phi^4_{3/2} & 0 & .. & .. & .. & .. & .. \\ .. & .. & .. & .. & .. & .. & .. & .. & .. & .. \\ .. & .. & 0 & \lambda^1_{k+1/2} & \lambda^2_{k+1/2} & \lambda^3_{k+1/2} & \lambda^4_{k+1/2} & 0 & .. & .. \\ .. & .. & 0 & \phi^1_{k+1/2} & \phi^2_{k+1/2} & \phi^3_{k+1/2} & \phi^4_{k+1/2} & 0 & .. & .. \\ .. & .. & .. & .. & .. & .. & .. & .. & .. & .. \\ .. & .. & .. & .. & .. & 0 & \lambda^1_{n-1/2} & \lambda^2_{n-1/2} & \lambda^3_{n-1/2} & \lambda^4_{n-1/2} \\ .. & .. & .. & .. & .. & 0 & \phi^1_{n-1/2} & \phi^2_{n-1/2} & \phi^3_{n-1/2} & \phi^4_{n-1/2} \end{pmatrix}, \tag{35}$$

$$\mathcal{S}=\begin{pmatrix} -\mu^1_{3/2} & -\mu^2_{3/2} & .. & .. & .. & .. & .. & .. & -\mu^{nj-1}_{3/2} & -\mu^{nj}_{3/2} \\ -\nu^1_{3/2} & -\nu^2_{3/2} & .. & .. & .. & .. & .. & .. & -\nu^{nj-1}_{3/2} & -\nu^{nj}_{3/2} \\ .. & .. & .. & .. & .. & .. & .. & .. & .. & .. \\ -\mu^1_{k+1/2} & -\mu^2_{k+1/2} & .. & .. & .. & .. & .. & .. & -\mu^{nj-1}_{k+1/2} & -\mu^{nj}_{k+1/2} \\ -\nu^1_{k+1/2} & -\nu^2_{k+1/2} & .. & .. & .. & .. & .. & .. & -\nu^{nj-1}_{k+1/2} & -\nu^{nj}_{k+1/2} \\ .. & .. & .. & .. & .. & .. & .. & .. & .. & .. \\ -\mu^1_{n-1/2} & -\mu^2_{n-1/2} & .. & .. & .. & .. & .. & .. & -\mu^{nj-1}_{n-1/2} & -\mu^{nj}_{n-1/2} \\ -\nu^1_{n-1/2} & -\nu^2_{n-1/2} & .. & .. & .. & .. & .. & .. & -\nu^{nj-1}_{n-1/2} & -\nu^{nj}_{n-1/2} \end{pmatrix}, \tag{36}$$

$\mathcal{I}$ the identity matrix and

$$\hat{P}=\begin{pmatrix} \hat{p}_1 \\ \hat{u}_1 \\ \vdots \\ \hat{p}_n \\ \hat{u}_n \end{pmatrix}, \qquad \hat{P}^f=\begin{pmatrix} \hat{P}^+_{1f} \\ 0 \\ \vdots \\ 0 \\ \hat{P}^-_{nf} \end{pmatrix}, \qquad \hat{\sigma}^0=\begin{pmatrix} \hat{\sigma}^0_1 \\ \vdots \\ \hat{\sigma}^0_{nj} \end{pmatrix}, \qquad \hat{\sigma}^f=\begin{pmatrix} \hat{\sigma}^f_1 \\ \vdots \\ \hat{\sigma}^f_{nj} \end{pmatrix}. \tag{37}$$

In Eq. (34), $\hat{P}$ and $\hat{\sigma}^0$ are the vectors of unknowns. $\mathcal{A}$ describes the mean flow inside the geometry, $\mathcal{S}$ corresponds to the acoustic source terms related to entropy fluctuations and $\hat{P}^f$ and $\hat{\sigma}^f$ represent the acoustic and entropy forcings imposed at the boundaries of the domain. Resolution of Eq. (34) provides the pressure and velocity fluctuations at each node of the nozzle, in particular at the geometry inlet and outlet. Acoustic and thermoacoustic transfer functions are then reconstructed using Eqs. (1) and (2).

3.2. Choked nozzle flow

When the mass flow rate is sufficiently large, the flow becomes choked and the velocity is supersonic in the diffuser. The modelling of choked nozzle flows is very similar to subsonic flows. Eqs. (13)-(14) (matrices $\mathcal{A}$ and $\mathcal{S}$) and Eq. (32) (upstream acoustic boundary condition) are unchanged and the only difference comes from the outlet boundary condition. As the flow is now supersonic at the outlet, the wave P_n^- leaves the domain and cannot be imposed anymore so that Eq. (33) does not hold. However, a unique property of choked flows is that the Mach number is 1 at nozzle throat, where the section is minimum [33,43]. The fluctuation of the section-averaged Mach number writes in linear regime

$$\overline{\left(\frac{M'}{M_0}\right)}=-\overline{\left(\frac{\gamma-1}{2\gamma p_0}\right)}p'+\overline{\left(\frac{1}{u_0}\right)}u'_x-\frac{1}{2}\overline{\left(\frac{s'}{c_p}\right)}. \tag{38}$$

Applying the condition $\overline{M'/M_0}=0$ at nozzle throat, Eq. (33) is replaced by Eq. (39) for choked nozzle flows:

$$-\overline{\left(\frac{\gamma-1}{2\gamma p_0}\right)}_t\hat{p}+\overline{\left(\frac{1}{u_0}\right)}_t\hat{u}-\frac{1}{2}\overline{\hat{\sigma}}_t=0, \tag{39}$$

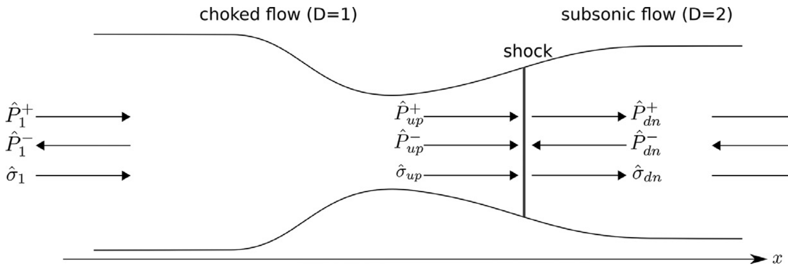

Fig. 2. Modelling of the supercritical nozzle with a shock in the diffuser.

where the index t indicates the node located at nozzle throat, where $\overline{M}_{0,t} = 1$. The system finally writes

$$\begin{pmatrix} \left(\frac{1}{2\gamma\overline{p}_0}\right)_1 & \left(\frac{\overline{\rho_0 c_0}}{2\gamma\overline{p}_0}\right)_1 & 0 & .. & .. & .. & .. & .. & .. & .. \\ & & & & & & \mathcal{A} & & & \mathcal{S} \\ .. & .. & 0 & -\overline{\left(\frac{\gamma-1}{2\gamma p_0}\right)}_t & -\overline{\left(\frac{1}{u_0}\right)}_t & 0 & .. & & & c\mathcal{C}_t \\ .. & .. & .. & .. & .. & .. & 0 & & & \\ \vdots & & & & & & \vdots & & & \mathcal{I} \\ .. & .. & .. & .. & .. & .. & 0 & & & \end{pmatrix} \begin{pmatrix} \hat{P} \\ [6pt] \\ \hat{\sigma}^0 \end{pmatrix} = \begin{pmatrix} \hat{p}^f \\ \\ \hat{\sigma}^f \end{pmatrix} \tag{40}$$

with

$$\mathcal{C}_t = \left(-\frac{A_1}{2A}e^{i\varphi_{t,1}} \quad \dots \quad -\frac{A_{nj}}{2A}e^{i\varphi_{t,nj}}\right)_t \tag{41}$$

and $\hat{P}_{nf}^- = 0$. In the same way as for the subsonic configuration, resolution of Eq. (40) provides the acoustic and thermoacoustic transfer functions of the nozzle flow.

3.3. Choked nozzle flow with a shock

When the back pressure imposed at nozzle outlet does not correspond to the discharge pressure of the choked nozzle, the flow is not adapted and shocks appear in the flow. If the back pressure is sufficiently large compared to the discharge pressure, a shock forms inside the diffuser after which the flow is subsonic. Upstream and downstream of the shock, the modelling of choked and subsonic nozzle flows are valid, so that a flow with a shock can be modelled as a combination of a choked nozzle flow and a subsonic nozzle flow separated by a normal shock. This configuration is depicted in Fig. 2, where the choked flow is referred to as domain 1 and the subsonic nozzle flow as domain 2 and where indices $(\,\cdot\,)_{up}$ and $(\,\cdot\,)_{dn}$ correspond to quantities taken just upstream and downstream of the shock. The only difference with the previous cases is that the progressive acoustic wave $\hat{P}_{dn}^+$ and entropy wave $\hat{\sigma}_{dn}$ at the upstream extremity of domain 2 (just downstream of the shock) are not imposed by the user but are additional unknowns that need to be determined during the resolution process. These perturbations are determined by solving dynamic shock relations. In this paper, the dynamic shock relations derived by Moase et al. [27] for quasi-1D flows are used. These relations link pressure, axial velocity and entropy fluctuations through the shock and write

$$\begin{aligned} &\frac{1}{1+\frac{\gamma-1}{2}M_{0,up}^2}\left[\left(\gamma-1-\left(M_{0,up}^2-\frac{\gamma-1}{2}\right)M_{0,dn}^2\frac{E_u}{E_p}\right)\frac{\hat{p}_{up}}{\gamma p_{0,up}}-\left(1-\frac{\gamma-1}{2}M_{0,up}^2+2M_{0,up}^2M_{0,dn}^2\frac{E_u}{E_p}\right)\frac{\hat{u}_{up}}{u_{0,up}}\right. \\ &\quad\left.+\left(1+M_{0,up}^2M_{0,dn}^2\frac{E_u}{E_p}\right)\frac{\hat{s}_{up}}{c_p}\right] = -\frac{E_u}{E_p}\frac{\hat{p}_{dn}}{\gamma p_{0,dn}}+\frac{\hat{u}_{dn}}{u_{0,dn}}, \end{aligned} \tag{42}$$

$$-\frac{1}{1+\frac{\gamma-1}{2}M_{0,up}^2}\left[\left(2-\gamma+\frac{\gamma-1}{2}M_{0,up}^2-\left(M_{0,up}^2-\frac{\gamma-1}{2}\right)M_{0,dn}^2\frac{E_\rho}{E_p}\right)\frac{\hat{p}_{up}}{\gamma p_{0,up}}+2\left(1-M_{0,up}^2M_{0,dn}^2\frac{E_\rho}{E_p}\right)\frac{\hat{u}_{up}}{u_{0,up}}\right.$$

$$+\left(M_{0,up}^2 M_{0,dn}^2 \frac{E_\rho}{E_p} - \left(2 + \frac{\gamma - 1}{2} M_{0,up}^2\right)\right) \frac{\hat{s}_{up}}{c_p}\Bigg] = -\left(1 - \frac{E_\rho}{E_p}\right) \frac{\hat{p}_{dn}}{\gamma p_{0,dn}} + \frac{\hat{s}_{dn}}{c_p}, \tag{43}$$

with

$$E_p = \frac{(1+\gamma^2) M_{0,up}^2 + \gamma - 1}{2\gamma M_{0,up}^2 - \gamma + 1} \left(1 - M_{0,up}^2\right) + 2 \frac{u_{0,dn}}{u_{0,up}} M_{0,up}^2 i\Omega_{dn}, \tag{44}$$

$$E_u = -\gamma \left(1 - M_{0,up}^2\right) - \frac{u_{0,dn}}{u_{0,up}} \frac{1 + M_{0,up}^2}{M_{0,dn}^2} i\Omega_{dn}, \tag{45}$$

$$E_\rho = \gamma \left(1 - M_{0,up}^2\right) + \frac{2u_{0,dn}}{u_{0,up} M_{0,dn}^2} i\Omega_{dn}, \tag{46}$$

and where $\Omega = \omega / (\partial u_{0x} / \partial x)$ is the nondimensional angular frequency.

Downstream of the shock, there are $nj + 1$ waves travelling in the downstream direction (*nj* being the number of streamtubes). There are therefore $nj + 1$ additional unknowns which require $nj + 1$ additional equations to close the system. Equation (42) is averaged over the section using Eq. (3) and Eq. (43) is solved for each streamtube, which provides $nj + 1$ equations. These equations write

$$\kappa^1 \hat{p}_{up} + \kappa^2 \hat{u}_{up} + \kappa^3 \hat{p}_{dn} + \kappa^4 \hat{p}_{dn} + \sum_j^{nj} \kappa^{5,j} \sigma_j^0 (D = 1) = 0, \tag{47}$$

$$\eta^{1,j} \hat{p}_{up} + \eta^{2,j} \hat{u}_{up} + \eta^{3,j} \hat{p}_{dn} + \eta^{5,j} \sigma_j^0 (D = 1) + \eta^{6,j} \sigma_j^0 (D = 2) = 0, \tag{48}$$

with

$$\kappa^1 = \overline{\left(\frac{1}{1 + \frac{\gamma-1}{2} M_{0,up}^2} \frac{1}{\gamma p_{0,up}} \left[\gamma - 1 - \left(M_{0,up}^2 - \frac{\gamma - 1}{2}\right) M_{0,dn}^2 \frac{E_u}{E_p}\right]\right)}, \tag{49}$$

$$\kappa^2 = -\overline{\left(\frac{1}{1 + \frac{\gamma-1}{2} M_{0,up}^2} \frac{1}{u_{0,up}} \left[1 - \frac{\gamma - 1}{2} M_{0,up}^2 + 2 M_{0,up}^2 M_{0,dn}^2 \frac{E_u}{E_p}\right]\right)}, \tag{50}$$

$$\kappa^3 = \overline{\left(\frac{1}{\gamma p_{0,dn}} \frac{E_u}{E_p}\right)}, \tag{51}$$

$$\kappa^4 = -\overline{\left(\frac{1}{u_{0,dn}}\right)}, \tag{52}$$

$$\kappa^{5,j} = \left(\frac{A_j}{A} \frac{1}{1 + \frac{\gamma-1}{2} M_{0,up}^2} \left[1 + M_{0,up}^2 M_{0,dn}^2 \frac{E_u}{E_p}\right]\right)_j e^{i\varphi_{up,j}}, \tag{53}$$

$$\eta^{1,j} = -\left(\frac{1}{1 + \frac{\gamma-1}{2} M_{0,up}^2} \frac{1}{\gamma p_{0,up}} \left[2 - \gamma + \frac{\gamma - 1}{2} M_{0,up}^2 - \left(M_{0,up}^2 - \frac{\gamma - 1}{2}\right) M_{0,dn}^2 \frac{E_\rho}{E_p}\right]\right)_j, \tag{54}$$

$$\eta^{2,j} = -\left(\frac{2}{1 + \frac{\gamma-1}{2} M_{0,up}^2} \frac{1}{u_{0,up}} \left[1 - M_{0,up}^2 M_{0,dn}^2 \frac{E_\rho}{E_p}\right]\right)_j, \tag{55}$$

$$\eta^{3,j} = \left(\frac{1}{\gamma p_{0,dn}} \left[1 - \frac{E_\rho}{E_p}\right]\right)_j, \tag{56}$$

$$\eta^{5,j} = -\left(\frac{1}{1 + \frac{\gamma-1}{2} M_{0,up}^2} \left[M_{0,up}^2 M_{0,dn}^2 \frac{E_\rho}{E_p} - \left(2 + \frac{\gamma - 1}{2} M_{0,up}^2\right)\right]\right)_j e^{i\varphi_{up,j}}, \tag{57}$$

$$\eta^{6,j} = -1. \tag{58}$$

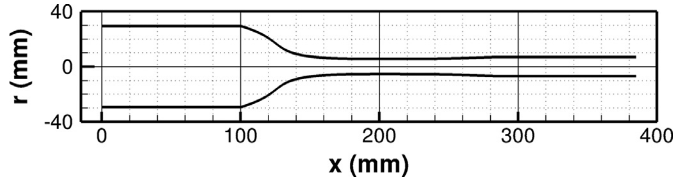

Fig. 3. Illustration of the nozzle used for the numerical validations.

The system finally writes in the presence of a shock in the diffuser

$$
\left(\begin{array}{ccccccccccccc}
\left(\frac{1}{2\gamma\bar{p}_0}\right)_1 & \left(\frac{\overline{\rho_0 c_0}}{2\gamma\bar{p}_0}\right)_1 & 0 & .. & .. & .. & .. & .. & .. & .. & .. & .. & .. \\
 & & & \mathcal{A}(D=1) & & & & & & \mathcal{S}(D=1) & & & 0 \\
 & & & & & & \mathcal{A}(D=2) & & & 0 & & & \mathcal{S}(D=2) \\
.. & .. & 0 & -\overline{\left(\frac{\gamma-1}{2\gamma p_0}\right)}_t & -\overline{\left(\frac{1}{u_0}\right)}_t & 0 & .. & & & \mathcal{C}_t & 0 & .. & .. \\
.. & .. & .. & .. & 0 & \left(\frac{1}{2\gamma\bar{p}_0}\right)_n & -\left(\frac{\overline{\rho_0 c_0}}{2\gamma\bar{p}_0}\right)_n & 0 & .. & .. & .. & .. & .. \\
.. & .. & .. & .. & .. & .. & 0 & & & & 0 & .. & .. \\
\vdots & & & & & & \vdots & & & \mathcal{I} & \vdots & & \vdots \\
.. & .. & .. & .. & .. & .. & 0 & & & & 0 & .. & .. \\
 & & & & & & \mathcal{K} & & & & & & \mathcal{H}
\end{array}\right)
$$

$$
\begin{pmatrix} \hat{P} \\ \\ \hat{\sigma}^0(D=1) \\ \\ \hat{\sigma}^0(D=2) \end{pmatrix} = \begin{pmatrix} \hat{P}^f \\ \\ \hat{\sigma}^f \\ 0 \\ \vdots \\ 0 \end{pmatrix} \tag{59}
$$

with

$$
\mathcal{K} = \begin{pmatrix}
.. & 0 & \kappa^1 & \kappa^2 & \kappa^3 & \kappa^4 & 0 & .. \\
.. & 0 & \eta^{1,1} & \eta^{2,1} & \eta^{3,1} & 0 & .. & .. \\
 & & \vdots & \vdots & \vdots & & & \\
 & & \vdots & \vdots & \vdots & & & \\
.. & 0 & \eta^{1,nj} & \eta^{2,nj} & \eta^{3,nj} & 0 & .. & ..
\end{pmatrix} \tag{60}
$$

and

$$
\mathcal{H} = \begin{pmatrix}
\kappa^{5,1} & .. & .. & \kappa^{5,nj} & 0 & .. & .. & .. \\
\eta^{5,1} & 0 & .. & 0 & \eta^{6,1} & 0 & .. & .. \\
0 & \ddots & 0 & .. & 0 & \ddots & 0 & .. \\
.. & 0 & \ddots & 0 & .. & 0 & \ddots & 0 \\
.. & .. & 0 & \eta^{5,nj} & 0 & .. & 0 & \eta^{6,nj}
\end{pmatrix}. \tag{61}
$$

Resolution of Eq. (3.3) provides the acoustic and thermoacoustic transfer functions of the nozzle.

4. Numerical validation

4.1. Test case

The geometry considered for the validation is a converging-diverging nozzle designed in the frame of the European-FP7 project RECORD to investigate indirect combustion noise and already used by Emmanuelli et al. for the validation of CHEOPS-Nozzle in the subsonic regime [38]. This nozzle is illustrated in Fig. 3. The nozzle in itself is 185 mm long, starting at $x = 100$ mm. It is completed upstream and downstream with ducts of constant section that are used to perform acoustic

Table 1
Main physical parameters of the test case.

Inlet Mach	Throat Mach	Outlet Mach	Inlet pressure	Outlet pressure
0.0203	1.00	0.428	120000 Pa	101325 Pa

waves separation. The flow is strongly accelerated in the converging part of the nozzle, where the radius reduces from 29.5 mm at the inlet to 5.5 mm at the throat, located at $x = 200$ mm. The diverging section is 85 mm long and the outlet radius is 6.943 mm. This ensures a low diverging angle in order to avoid flow separation.

The operating point considered is summarised in Table 1. It corresponds to a choked configuration with a shock in the diffuser, located at $x = 251.8$ mm. The inlet temperature is set to 1300 K to be representative of flow conditions at the exit of a combustion chamber and the gas considered is air with a heat capacity ratio γ of 1.315.

4.2. Methodology

The methodology follows the work of Emmanuelli et al. [38]. Planar entropy and acoustic waves are considered for the forcings. The 2D model requires inviscid mean flow fields that are computed with the CFD (Computational Fluid Dynamics) code CEDRE from ONERA [44]. Validations are performed through comparisons of the modelled transfer functions with reference results obtained numerically with 3D CAA simulations. These simulations are run with the flow solver *sAbrinA_v0* from ONERA [45,46]. The nonlinear Euler equations are solved in the time domain with a perturbation form of the conservative variables made of the mean flow and a disturbance field. A standard sixth order finite difference scheme is used in space to limit numerical dispersion and dissipation effects [47,48], combined with a standard tenth order explicit filtering to remove numerical oscillations near the cut-off frequency [48,49], and a third order explicit compact Runge-Kutta scheme is applied in time [50,51]. Efficient numerical boundary conditions derived by Tam et al. [52,53] from the asymptotic solutions of the linearised Euler equations are applied to provide almost non reflective boundary conditions and to allow the injection of entropy and acoustic waves through the boundaries. The mesh is 3D structured and composed of 2.2×10^6 nodes. The mesh is dimensioned to have at least 18 points per acoustic or entropic wavelength at 1000 Hz, the highest supported frequency considered. A time step of 4×10^{-8} s is chosen so that the CFL lies below 0.50. To end, the same mean flow field is used for the model and the CAA simulations.

The computation of transfer functions from the CAA simulations requires the separation of the waves in the ducts upstream and downstream of the nozzle. The entropy wave σ is directly obtained from the entropy fluctuation using Eq. (1). Riemann invariants given in Eq. (2) are valid in the upstream duct but not in the downstream one, because in this duct a fraction of the velocity fluctuations is associated with vorticity waves generated inside the nozzle [34]. Acoustic waves are hence reconstructed using a mode matching method based on pressure fluctuations only [40,54]. Under the assumption that the pressure fluctuations are purely acoustic and one dimensional (which has been verified numerically), one can write in the harmonic regime:

$$p' = p'^{+} + p'^{-}, \tag{62}$$

$$\frac{\partial p'}{\partial x} = -ik_x^+ p'^{+} - ik_x^- p'^{-}, \tag{63}$$

with p'^{+} and p'^{-} the pressure fluctuations associated with the progressive and regressive acoustic waves, respectively, and k_x^+ and k_x^- their wavenumbers defined as

$$k_x^{\pm} = \frac{\omega}{u_{0x} \pm c_0}. \tag{64}$$

The left-hand-side terms of Eqs. (62)-(63) are provided by CAA and the wavenumbers are evaluated from the mean flow field, so that the system of Eqs. (62)-(63) can be solved to provide the amplitudes of the acoustic waves, that are normalised using Eq. (2) and finally write:

$$P^{\pm} = \frac{p'^{\pm}}{\gamma \overline{p}_0}. \tag{65}$$

Although the almost non reflective boundary conditions of Tam et al. [52,53] are used in the simulations, small acoustic reflexions can still occur on the domain boundaries and spurious pressure waves may propagate back to the nozzle and contaminate the simulations. To avoid the corruption of the nozzle transfer functions, numerical results are post-processed once the simulations with the three different forcings (entropic and upstream/downstream acoustic) are complete to reconstruct the transfer functions with transparent-like boundaries. Details on this post-processing are given in Emmanuelli et al. [38].

To end, a grid convergence study was successfully performed for the CAA and the model. Analytical transfer functions computed with 6, 12, 25 and 50 streamtubes are reproduced in Fig. 4 to illustrate the grid convergence of the model. Excellent convergence is obtained with 50 streamtubes and this value is used for all results presented hereafter. Of interest, the

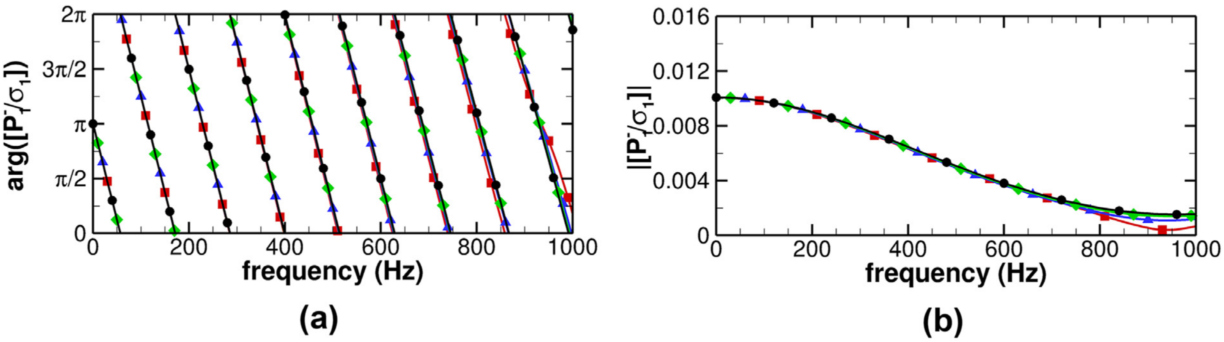

Fig. 4. Illustration of the convergence of the modelled thermoacoustic transfer function $[P_1^-/\sigma_1]$. (a) amplitude, (b) phase. ■— 6 streamtubes, ▲— 12 streamtubes, ♦— 25 streamtubes, •— 50 streamtubes.

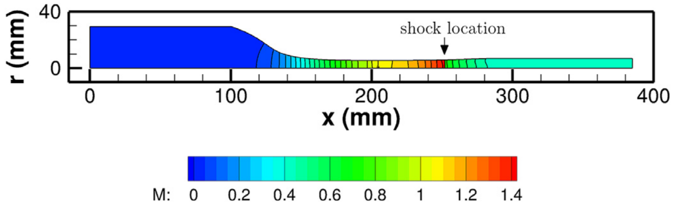

Fig. 5. Mean Mach number evolution along the nozzle.

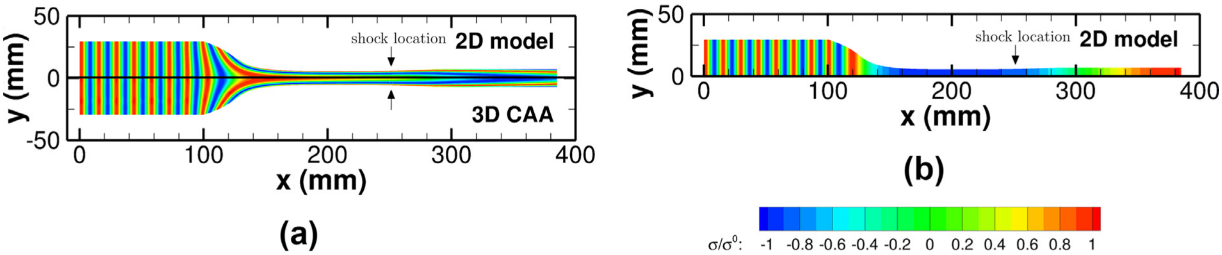

Fig. 6. Simulated and modelled entropy fluctuation at 1000 Hz through the nozzle. (a) 2D mean flow (2D model (50 streamtubes) and CAA), (b) quasi-1D mean flow (1 streamtube).

largest number of streamtubes is required to reach the convergence at high frequencies because the relative radial stretching of the entropy wave through the nozzle (in comparison to its wavelength) is the most important for such frequencies.

For the sake of completeness, the solutions provided by the 2D model Cheops-Nozzle for a quasi-1D flow (no radial dependence of the flow variables) are also evaluated and discussed in this section. These additional results are obtained by running the model with a quasi-1D mean flow and only one streamtube. It has been verified that the transfer functions obtained collapse with those predicted with the quasi-1D model Marcan of ONERA [28,29], as expected (comparisons not shown).

4.3. Numerical results

The evolution of the mean Mach number along the nozzle, computed with CEDRE and used as input data for the 2D model and the 3D CAA, is illustrated in Fig. 5. As a first validation, the entropy fluctuation both computed and modelled at 1000 Hz using the 2D mean flow is reproduced in Fig. 6 (a). The modelled entropy is identical to the computed one, which validates the entropy convection performed in CHEOPS-Nozzle. The deformation of the entropy wave is clearly visible in this figure and outlines the limit of the quasi-1D approach. The shear dispersion of the entropy wave is caused by the 2D nature of the mean velocity field, in particular at the nozzle entrance, along with the longer convection distance to pass through the nozzle for an entropy spot located near the nozzle wall compared to a perturbation on the axis. This dispersion is well illustrated near the nozzle throat, where the entropy wavefront on the axis catches up with the preceding wavefront at the wall, resulting in an important radial variation of the entropy fluctuation. As a comparison, the entropy fluctuation computed with the quasi-1D approach is reproduced in Fig. 6 (b). By definition, shear dispersion is not captured with this approach and the entropy wave remains planar. The discrepancy between the quasi-1D and 2D solutions is visible along the whole nozzle and illustrates the failure of the quasi-1D approach to accurately model the generation of entropy noise.

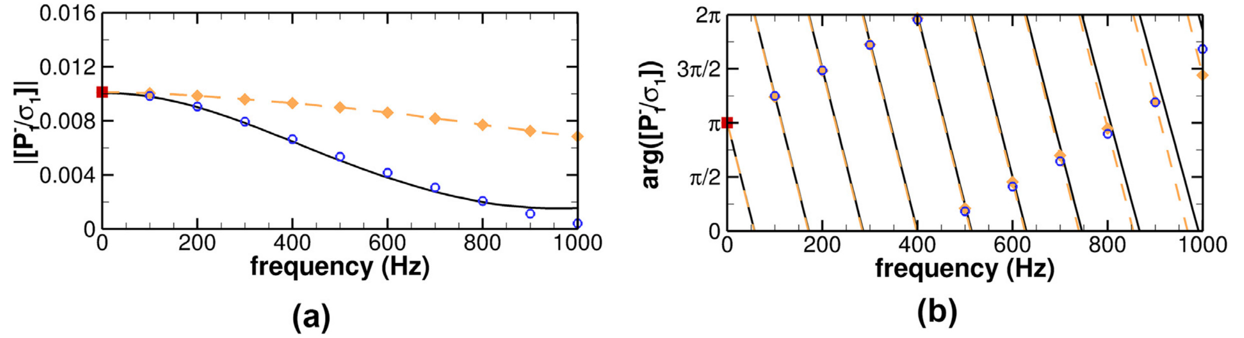

Fig. 7. Simulated and modelled thermoacoustic transfer function $[P_1^-/\sigma_1]$. (a) amplitude, (b) phase. ■ Compact solution [25]; ◆ – – CHEOPS-Nozzle with quasi-1D flow field; — CHEOPS-Nozzle with 2D flow field; ○ CAA simulations.

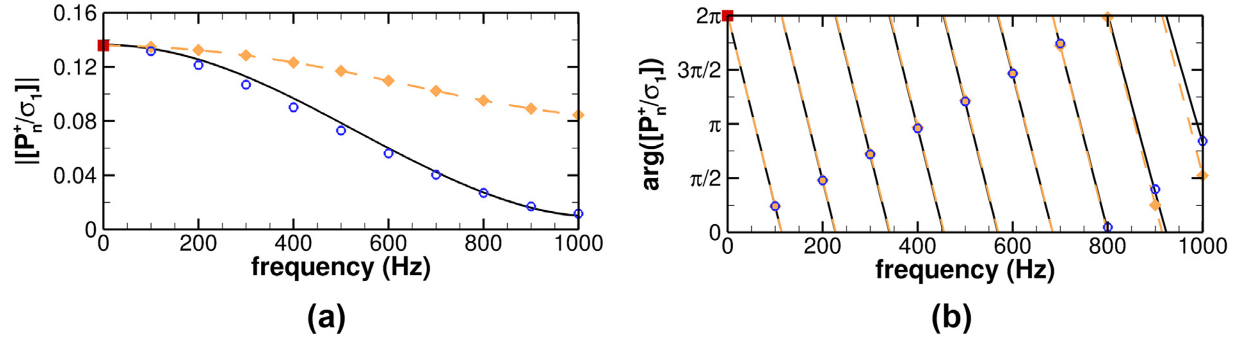

Fig. 8. Simulated and modelled thermoacoustic transfer function $[P_n^+/\sigma_1]$. (a) amplitude, (b) phase. See Fig. 7 for legend.

Next, the computed and modelled thermoacoustic transfer functions are reproduced in Figs. 7 and 8, for the upstream and downstream generated acoustic waves respectively. These figures reproduce the compact solutions valid in the low-frequency limit [25], the non-compact solution modelled with the quasi-1D mean flow, the non-compact solution modelled with the 2D mean flow and the transfer functions obtained with CAA. Analyses are similar for both figures.

Very good agreement is observed between the reference CAA data and the 2D model Cheops-Nozzle when the 2D flow field is considered, for both amplitude and phase, despite the slight overestimation of the generated noise with the model for $[P_1^-/\sigma_1]$ and frequencies above 900 Hz. This overestimation may come from the contribution of vorticity that is neglected in the model. However, the similarity of the analytical and numerical 2D results over most of the frequency range indicates that the contribution of vorticity to noise generation remains very limited. The modelled transfer functions also collapse with the compact solutions in the low-frequency limit, as expected. The analytical solution with the quasi-1D mean flow field collapses with the other approaches for low frequencies, where the radial distortion of the entropy wave remains limited due to the very large entropy wavelengths. As the frequency increases, however, differences rapidly rise between the quasi-1D solution and the 2D solutions because of the distortion of the entropy wave. The noise source term being the product between the entropy fluctuation and the mean flow gradient (see Marble and Candel [19] and Eq. (10)), the deformation of the entropy wave leads to a radial decorrelation of the local source terms which reduces the generated noise, hence the overestimation of the quasi-1D solution compared to the 2D transfer functions. A similar observation was made in the subsonic regime [38]. Of interest, in the present case the nozzle is choked so that the pressure perturbations present in the divergent zone cannot propagate back to the convergent region and the generated wave P_1^- is produced exclusively by the flow upstream of the nozzle throat. The strong differences between the quasi-1D and 2D modelled transfer functions, visible in Fig. 7 (a), indicate that the alteration of the entropy noise sources caused by the shear dispersion in the convergent of the nozzle is very important, as already inferred from Fig. 6. Finally, it is worth noting that the major differences concern the amplitude of the transfer functions while the phase variations between the quasi-1D and 2D approaches remain negligible. The phase-shift term is the consequence of the convection time of the entropy wave and propagation time of the acoustic waves through the nozzle. Despite the important deformation of the entropy wave and its phase-lag between nozzle axis and walls for the 2D model, it has been verified that the phase of the section-averaged entropy fluctuation is very similar between the 2D and quasi-1D configurations, hence the similar phase results.

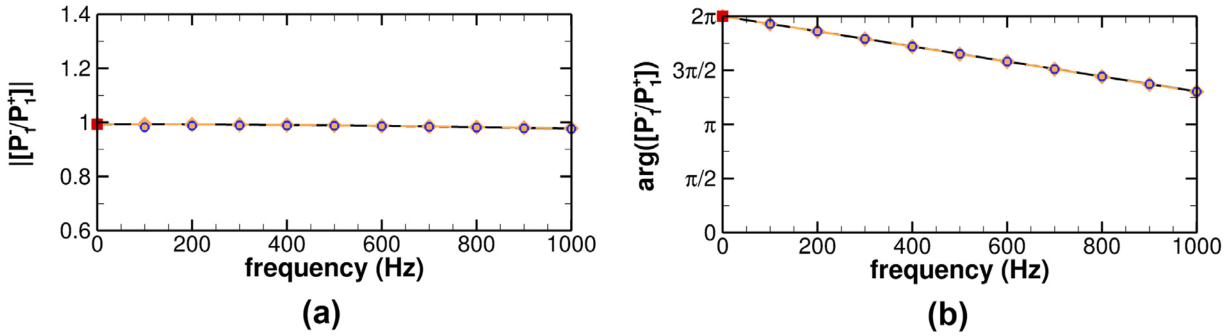

Fig. 9. Simulated and modelled thermoacoustic transfer function $[P_1^-/P_1^+]$. (a) amplitude, (b) phase. See Fig. 7 for legend.

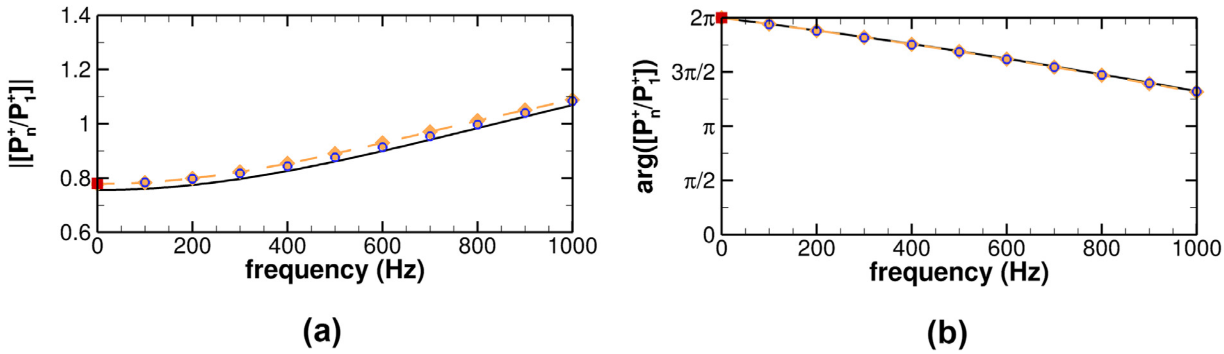

Fig. 10. Simulated and modelled thermoacoustic transfer function $[P_n^+/P_1^+]$. (a) amplitude, (b) phase. See Fig. 7 for legend.

To complement these results, the acoustic transfer functions of the nozzle, corresponding to the noise scattered through the nozzle when acoustic waves enter from either upstream or downstream, are reproduced in Figs. 9–11. The nozzle being choked, no information can propagate from the exit to the inlet, therefore $[P_1^-/P_n^-] = 0$ and this transfer function is not reproduced in the article.

Fig. 9 corresponds to the acoustic wave reflected by the nozzle in the case of a forcing from the inlet. Both quasi-1D and 2D models are in excellent agreement with the CAA results and the theoretical compact solution [19,25]. The agreement between CAA and the 2D model confirms in particular that the acoustic waves remain essentially planar inside the nozzle, as assumed in the model. This hypothesis has also been directly verified from the computed pressure fields, not reproduced here. In addition, the identical modelled results obtained using quasi-1D and 2D mean flow indicate that the 2D mean flow variations have no consequence on the scattering of the acoustic waves [38]. Moreover, the evolution of the transfer function with frequency is very low: amplitude does not significantly vary and the phase shifts only by $3\pi/4$ between 0 and 1000 Hz. This result is a consequence of the short axial dimension of the convergent section of the nozzle, $l_c = 100$ mm, in comparison to the acoustic wavelengths λ_P ($\lambda_P \sim 700$ mm at 1000 Hz in the upstream duct), so that the convergent is essentially compact ($\lambda_P/l_c \gg 1$) for acoustic perturbations. Note that the nozzle cannot be considered as compact for entropy forcing because the convection velocity is very low in the upstream duct. Hence, entropy wavelengths are shorter than or similar to the length of the convergent section ($\lambda_\sigma \sim 14$ mm at 1000 Hz) and variations of the thermoacoustic transfer function are strong, as observed in Fig. 7. The non compactness of the nozzle for entropy forcing is also visible in Fig. 6 (a).

The transfer function associated with the acoustic wave transmitted through the nozzle from the upstream end to the downstream end is reproduced in Fig. 10. Once again, very good agreement is observed between the modelled solutions and CAA results, despite slight differences between Cheops-Nozzle using quasi-1D and 2D mean flow fields. This discrepancy corresponds to an underprediction of the transfer function with Cheops-Nozzle and the 2D mean flow, as the model does not recover the compact solution in the low frequency limit. It is a consequence of the difficult evaluation of the mean axial velocity gradient near the shock in the 2D aerodynamic simulation, and numerical investigations evidenced some slight variations in the modelled transfer functions when different flow field interpolation procedures are used to generate the input data for the model. This discrepancy however lies below 3% and can be considered as negligible in the scope of indirect noise prediction inside an engine. To end with this figure, it can be observed that the transfer function for the transmitted acoustic wave exhibits more variations than that of the reflected wave, with an increase of about 40% of its

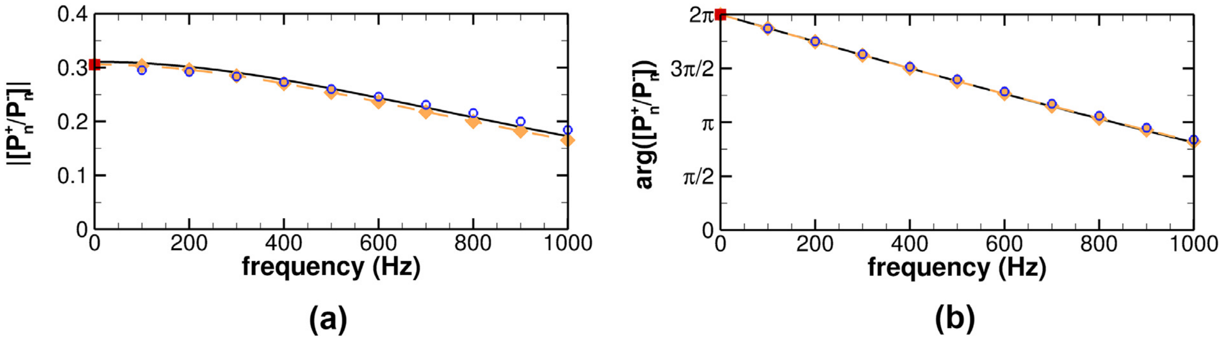

Fig. 11. Simulated and modelled thermoacoustic transfer function $[P_n^+/P_n^-]$. (a) amplitude, (b) phase. See Fig. 7 for legend.

amplitude between 0 and 1000 Hz. This can be attributed to two origins. First, for the present case the acoustic waves cross the whole nozzle, which reduces the validity of the compactness criterion in particular for large frequencies. Second, the acoustic waves travel through the shock and the response of the shock to this forcing depends on the frequency, see Eqs. (44)-(46), so that even if the nozzle can be considered as compact in the regions upstream and downstream of the shock, the response of the shock itself to the incoming acoustic waves may modulate the transfer function with frequency.

Finally, the transfer function of the acoustic wave reflected by the nozzle with a forcing from the outlet is illustrated in Fig. 11. As for the previous acoustic transfer functions, the agreement is very good between the compact solution, Cheops-Nozzle modelled transfer functions and CAA results. Because the nozzle is choked, only the subsonic part of the flow in the divergent region of the nozzle, $x \geq 251.8$ mm, contritubes to the reflection of the acoustic waves. The acoustic wavelength λ_P lies above 200 mm in this region at 1000 Hz whereas the subsonic part of the divergent is $l_{d,sub} = 33.2$ mm, so that the compact criterion globally holds. The variation in the amplitude of the transfer function with frequency hence comes from the response of the shock to the impinging retrograde acoustic wave, as discussed above. The higher the frequency the lower the reflection of the acoustic wave, which seems to indicate that for this configuration the dissipation of the acoustic energy by the shock rises as the frequency increases. This result is similar to the experimental and numerical observations on the HAT nozzle [21,36].

From a numerical point of view, the evaluation of the thermoacoustic transfer functions with CAA (10 frequencies from 100 Hz to 1000 Hz) requires approximatively 16,000 hours of computational time, whereas these transfer functions are evaluated within only 15 seconds with the analytical model. Despite some possible optimisations in the CAA process (2D simulations would drastically decrease the computational time, for instance), the model will always remain much faster and appears very well suited for inclusion in an optimization process such as low-noise shape design, as done for instance by Giauque et al. [30] with a quasi-1D model. The 2D model seems mature enough for such a thermoacoustic optimisation, even if the inviscid flow considered remains relatively simple. Some improvements are still possible to aim towards more realistic flow physics if the impact on noise generation is evidenced. The major limitation of the current model is the inviscid assumption, as boundary layers might be significant in such wall-bounded configurations. Such boundary layers are expected to enhance shearing of entropy fluctuations near the walls and possibly impact noise generation.

5. Conclusions

The 2D model developed at ONERA for the computation of indirect combustion noise through a subsonic nozzle [38] is extended in the present article to choked nozzles flows, without and with a shock in the diffuser. This model differs from the quasi-1D approaches available in the literature by taking into account the radial deformation of the entropy fluctuations by the mean flow during their convection through the nozzle. The numerical resolution is performed by considering planar acoustic perturbations inside the nozzle, a normal shock in the diffuser and by neglecting vorticity fluctuations. The flow equations are derived in the first part of the article from the Euler equations before being linearised and recast for numerical resolution. The model is then validated for a choked flow configuration with a shock in the diffuser through comparisons with reference data obtained with CAA simulations. Excellent agreement is observed between the 2D model and CAA results for all the forcings considered and the compact solution of Marble and Candel [19] is correctly recovered by the model as well. With entropy forcing, 2D transfer functions collapse well with the quasi-1D solution classically used in the literature [28,29,31–33] in the low frequency range but discrepancies increase as frequency rises because the radial distortion of the entropy wave is not taken into account by the quasi-1D approach. Of interest, quasi-1D modelled transfer functions collapse with CAA data in the case of acoustic forcings, which indicates that 2D mean flow effects are negligible for noise scattering through the nozzle.

Disclosure of conflicts of interest

The authors declare that they have no known competing financial interests or personal relationships that could have appeared to influence the work reported in this paper.

Declaration of Competing Interest

The authors declare that they have no known competing financial interests or personal relationships that could have appeared to influence the work reported in this paper.

Acknowledgements

This work is funded by ONERA. The authors are grateful to the CEDRE software team and in particular to Bernard Courbet for their help into the realization of the CFD simulation.

Appendix A. Noise generation in the presence of multiple forcings

In this appendix, an analytical method is proposed to determine the noise generated through the nozzle in practical configurations, such as cases with frequency-dependent forcings, simultaneous acoustic and entropy forcings or a non-isolated nozzle, that is to say when the waves leaving the nozzle domain produce additional acoustic waves that propagate back to the nozzle. It may correspond for instance to the use of experiment-based forcings, to the modelling of the presence of additional mechanical elements such as turbine stages upstream or downstream of the nozzle, or to numerical reflections on the domain boundaries in numerical simulations. The configuration is illustrated in Fig. A.1 where acoustic and entropy waves are represented at both extremities of the nozzle. In the harmonic regime, the transfer functions of the isolated nozzle (no reflections on the boundaries) write $\left[P_1^-/\sigma_1\right]$, $\left[P_1^-/P_1^+\right]$, ..., $\left[\sigma_n/P_n^-\right]$ and the additional forcing fluctuations generated by the waves leaving the domain are characterized by the reflections coefficients $R_{in}^{aa}=\left[P_1^+/P_1^-\right]$, $R_{in}^{as}=\left[\sigma_1/P_1^-\right]$, $R_{out}^{aa}=\left[P_n^-/P_n^+\right]$ and $R_{out}^{sa}=\left[P_n^-/\sigma_n\right]$. In the linear harmonic regime, the generated waves write in the general case:

$$\hat{P}_1^-=\left[\frac{P_1^-}{\sigma_1}\right]\hat{\sigma}_1+\left[\frac{P_1^-}{P_1^+}\right]\hat{P}_1^++\left[\frac{P_1^-}{P_n^-}\right]\hat{P}_n^-, \tag{A.1}$$

$$\hat{P}_n^+=\left[\frac{P_n^+}{\sigma_1}\right]\hat{\sigma}_1+\left[\frac{P_n^+}{P_1^+}\right]\hat{P}_1^++\left[\frac{P_n^+}{P_n^-}\right]\hat{P}_n^-, \tag{A.2}$$

$$\hat{\sigma}_n=\left[\frac{\sigma_n}{\sigma_1}\right]\hat{\sigma}_1+\left[\frac{\sigma_n}{P_1^+}\right]\hat{P}_1^++\left[\frac{\sigma_n}{P_n^-}\right]\hat{P}_n^-, \tag{A.3}$$

with

$$\hat{\sigma}_1=\hat{\sigma}_{1f}+R_{in}^{as}\hat{P}_1^-, \tag{A.4}$$

$$\hat{P}_1^+=\hat{P}_{1f}^++R_{in}^{aa}\hat{P}_1^-, \tag{A.5}$$

$$\hat{P}_n^-=\hat{P}_{nf}^-+R_{out}^{aa}\hat{P}_n^++R_{out}^{sa}\hat{\sigma}_n. \tag{A.6}$$

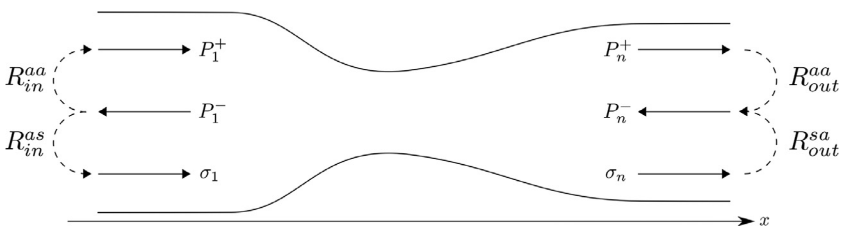

Fig. A.1. Sketch of the modelled nozzle with incoming and outgoing waves and upstream and downstream reflections.

It comes after some algebra the matrix system

$$\begin{pmatrix} 1-\left(R_{in}^{as}\left[\frac{P_1^-}{\sigma_1}\right]+R_{in}^{aa}\left[\frac{P_1^-}{P_1^+}\right]\right) & -R_{out}^{aa}\left[\frac{P_1^-}{P_n^-}\right] & -R_{out}^{sa}\left[\frac{P_1^-}{P_n^-}\right] \\ -\left(R_{in}^{as}\left[\frac{P_n^+}{\sigma_1}\right]+R_{in}^{aa}\left[\frac{P_n^+}{P_1^+}\right]\right) & 1-R_{out}^{aa}\left[\frac{P_n^+}{P_n^-}\right] & -R_{out}^{sa}\left[\frac{P_n^+}{P_n^-}\right] \\ -\left(R_{in}^{as}\left[\frac{\sigma_n}{\sigma_1}\right]+R_{in}^{aa}\left[\frac{\sigma_n}{P_1^+}\right]\right) & -R_{out}^{aa}\left[\frac{\sigma_n}{P_n^-}\right] & 1-R_{out}^{sa}\left[\frac{\sigma_n}{P_n^-}\right] \end{pmatrix}\begin{pmatrix}\hat{P}_1^- \\ \hat{P}_n^+ \\ \hat{\sigma}_n\end{pmatrix}$$

$$= \begin{pmatrix} \left[\frac{P_1^-}{\sigma_1}\right] & \left[\frac{P_1^-}{P_1^+}\right] & \left[\frac{P_1^-}{P_n^-}\right] \\ \left[\frac{P_n^+}{\sigma_1}\right] & \left[\frac{P_n^+}{P_1^+}\right] & \left[\frac{P_n^+}{P_n^-}\right] \\ \left[\frac{\sigma_n}{\sigma_1}\right] & \left[\frac{\sigma_n}{P_1^+}\right] & \left[\frac{\sigma_n}{P_n^-}\right] \end{pmatrix}\begin{pmatrix}\hat{\sigma}_{1f} \\ \hat{P}_{1f}^+ \\ \hat{P}_{nf}^-\end{pmatrix} \tag{A.7}$$

that can be easily solved to provide the complex amplitudes of the three generated waves $\hat{P}_1^-$, $\hat{P}_n^+$ and $\hat{\sigma}_n$.

References

[1] ACARE, Aeronautics and air transport: beyond vision 2020 (towards 2050), 2010, http://ec.europa.eu/research/transport/pdf/acare_background_2010_en.pdf
[2] W. Neise, L. Enghardt, Technology approach to aero engine noise reduction, Aerosp. Sci. Technol. 7 (2003) 352–363.
[3] A.P. Dowling, Y. Mahmoudi, Combustion noise, Proc. Combust. Inst. 35 (2015) 65–100.
[4] M. Ihme, Combustion and engine-core noise, Annu. Rev. Fluid Mech. 49 (2017) 277–310.
[5] Combustion Instabilities In Gas Turbine Engines: Operational Experience, Fundamental Mechanisms, and Modeling, in: T.C. Lieuwen, V. Yang (Eds.), Progress in Astronautics and Aeronautics, 210, AIAA, 2005.
[6] E. Motheau, F. Nicoud, T. Poinsot, Mixed acoustic-entropy combustion instabilities in gas turbines, J. Fluid Mech. 749 (2014) 542–576.
[7] W.C. Strahle, A review of combustion generated noise, in: Proceedings of the 1st AIAA Aeroacoustics Conference, AIAA Paper 73–1023, 1973.
[8] D.G. Crighton, The excess noise field of subsonic jets, J. Fluid Mech. 56 (1972) 683–694.
[9] N.A. Cumpsty, F.E. Marble, Core noise from gas turbine exhausts, J. Sound Vib. 54 (1977) 297–309.
[10] W.C. Strahle, Combustion noise, Prog. Energy Combust. Sci. 4 (1978) 157–176.
[11] S.L. Bragg, Combustion noise, J. Inst. Fuel 36 (1963) 12–16.
[12] W.C. Strahle, On combustion generated noise, J. Fluid Mech. 49 (1971) 399–414.
[13] W.C. Strahle, Some results in combustion generated noise, J. Sound Vib. 23 (1972) 113–125.
[14] H. Hassan, Scaling of combustion generated noise, J. Fluid Mech. 49 (1974) 445–453.
[15] S. Candel, Analytical Studies of Some Acoustic Problems of Jet Engines, California Institute of Technology, 1972 Ph.D. thesis.
[16] F.E. Marble, Acoustic disturbance from gas non-uniformities convecting through a nozzle, in: Proceedings of the Interagency Symposium on University Research in Transportation Noise, pp. 547–561, 1973.
[17] C.L. Morfey, Amplification of aerodynamic noise by convected flow inhomogeneities, J. Sound Vib. 31 (1973) 391–397.
[18] L. Magri, J. O'Brien, M. Ihme, Compositional inhomogeneities as a source of indirect combustion noise, J. Fluid Mech. 799 (2016) R4.
[19] F.E. Marble, S.M. Candel, Acoustic disturbance from gas non-uniformities convected through a nozzle, J. Sound Vib. 55 (1977) 225–243.
[20] F. Bake, C. Richter, B. Mühlbauer, N. Kings, I. Röhle, F. Thiele, B. Noll, The entropy wave generator (EWG): a reference case on entropy noise, J. Sound Vib. 326 (2009) 574–598.
[21] K. Knobloch, T. Werner, F. Bake, Noise generation in hot nozzle flow, in: Proceedings of ASME Turbo Expo 2015, Paper GT2015-43702, 2015.
[22] C.K.W. Tam, S.A. Parrish, The physical processes of indirect combustion noise generation, Int. J. Aeroacoust. 17 (2018) 22–35.
[23] C.K.W. Tam, F. Bake, L.S. Hultgren, T. Poinsot, Combustion noise: modeling and prediction, CEAS Aeronaut. J. 10 (2019) 101–122.
[24] M. Huet, A. Giauque, A nonlinear model for indirect combustion noise through a compact nozzle, J. Fluid Mech. 733 (2013) 268–301.
[25] M. Huet, Nonlinear indirect combustion noise for compact supercritical nozzle flows, J. Sound Vib. 374 (2016) 211–227.
[26] Y. Mahmoudi, A.P. Dowling, S. Stow, Combustion noise in an idealised combustor, in: Proceedings of the 25th International Colloquium on the Dynamics of Explosions and Reactive Systems, Paper 114, 2015.
[27] W.H. Moase, M.J. Brear, C. Manzie, The forced response of choked nozzles and supersonic diffusers, J. Fluid Mech. 585 (2007) 281–304.
[28] A. Giauque, M. Huet, F. Clero, Analytical analysis of indirect combustion noise in subcritical nozzles, J. Eng. Gas Turbine Power 134 (2012) 111202.
[29] M. Huet, F. Vuillot, N. Bertier, M. Mazur, N. Kings, W. Tao, P. Scouflaire, F. Richecoeur, S. Ducruix, C. Lapeyre, T. Poinsot, Recent improvements in combustion noise investigation: from the combustion chamber to nozzle flow, Aerosp. Lab 11 (2016).
[30] A. Giauque, M. Huet, F. Clero, S. Ducruix, F. Richecoeur, Thermoacoustic shape optimization of a subsonic nozzle, J. Eng. Gas Turbine Power 135 (2013) 102601.
[31] Y. Mahmoudi, A.P. Dowling, S.R. Stow, Acoustic and entropy waves in nozzles in combustion noise framework, AIAA J. 55 (2017) 2369–2381.
[32] M.S. Bohn, Response of a subsonic nozzle to acoustic and entropy disturbances, J. Sound Vib. 52 (1977) 283–297.
[33] I. Duran, S. Moreau, Solution of the quasi-one-dimensional linearized euler equations using flow invariants and the magnus expansion, J. Fluid Mech. 723 (2013) 190–231.
[34] I. Duran, A.S. Morgans, On the reflection and transmission of circumferential waves through nozzles, J. Fluid Mech. 773 (2015) 137–153.
[35] M. Huet, Influence of calorically perfect gas assumption and thermal diffusion on indirect noise generation, in: Proceedings of the 24th International Congress on Sound and Vibration, 2017.
[36] M. Huet, Budgets of disturbances energy for nozzle flows at subsonic and choked regimes, J. Eng. Gas Turbine Power 140 (2018) 112602.
[37] J. Zheng, M. Huet, F. Cléro, A. Giauque, S. Ducruix, A 2D-axisymmetric analytical model for the estimation of indirect combustion noise in nozzle flows, in: Proceedings of the 21st AIAA/CEAS Aeroacoustics Conference, AIAA Paper 2015–2974, 2015.

[38] A. Emmanuelli, J. Zheng, M. Huet, A. Giauque, T. Le Garrec, S. Ducruix, Description and application of a 2D-axisymmetric model for entropy noise in nozzle flows, J. Sound Vib. 472 (2020) 115163.
[39] J. Zheng, Analytical and Numerical Study of the Indirect Combustion Noise Generated by Entropy Disturbances in Nozzle Flows, Université Paris-Saclay, 2016 Ph.D. thesis.
[40] A. Emmanuelli, M. Huet, T. Le Garrec, S. Ducruix, CAA study of entropy noise in nozzle flow for the validation of a 2D semi-analytical model, in: Proceedings of ASME Turbo Expo 2017, Paper GT2017-63640, 2017.
[41] C. Becerril Aguirre, Simulation of Noise Emitted by a Reactive Flow, Institut National Polytechnique de Toulouse, 2017 Ph.D. thesis.
[42] B.-T. Chu, L.S.G. Kovásznay, Non-linear interactions in a viscous heat-conducting compressible gas, J. Fluid Mech. 3 (1958) 494–514.
[43] J.D. Anderson Jr., Modern Compressible Flow with Historical Perspective, 2nd, McGraw-Hill, 1990.
[44] A. Refloch, B. Courbet, A. Murrone, P. Villedieu, C. Laurent, P. Gilbank, J. Troyes, L. Tessé, G. Chaineray, J.B. Dargaud, E. Quémerais, F. Vuillot, CEDRE Software, Aerospace Lab 2 (2011).
[45] S. Redonnet, E. Manoha, P. Sagaut, Numerical simulations of propagation of small perturbations interacting with flows and solid bodies, in: Proceedings of the 7th AIAA/CEAS Aeroacoustics Conference, Paper 2001–2223, 2001.
[46] S. Redonnet, G. Desquesnes, E. Manoha, C. Parzani, Numerical study of acoustic installation effects with a computational aeroacoustics method, AIAA J. 48 (2010) 929–937.
[47] K.A. Hoffman, S.T. Chiang, S. Siddiqui, M. Papadakis, Fundamental equations of fluid mechanics, Eng. Educ.Syst., 1996.
[48] C. Bogey, C. Bailly, A family of low dispersive and low dissipative explicit schemes for flow and noise computations, J. Comput. Phys. 194 (2004) 194–214.
[49] S.K. Lele, Compact finite difference schemes with spectral-like resolution, J. Comput. Phys. 103 (1992) 16–42.
[50] G. Desquesnes, Couplage par Recouvrement de Maillages Curviligne/Cartésien pour la Simulation en aéroacoustique (An Overlapping Grid Methodology for Computational aeroacoustics), Université Pierre et Marie Curie, 2007 Ph.D. thesis.
[51] P.S. Lowery, W.C. Reynolds, Numerical Simulation of a Spatially-Developing, Forced, Plane Mixing Layer, Technical Report, Mech. Eng. Dept., Stanford University, 1986.
[52] C.K.W. Tam, J.C. Webb, Dispersion-relation-preserving finite difference schemes for computational acoustics, J. Comput. Phys. 107 (1993) 262–281.
[53] C.K.W. Tam, Z. Dong, Radiation and outflow boundary conditions for direct computation of acoustic and flow disturbances in a nonuniform mean flow, J. Comput. Acoust. 4 (1996) 175–201.
[54] S. Rienstra, A. Hirschberg, An Introduction to Acoustics, Eindhoven University of Technology, 2015.